ParaNet: Deep Regular Representation for 3D Point Clouds

Qijian Zhang[1]   Junhui Hou[1*]   Yue Qian[1]   Juyong Zhang[2]   Ying He[3]

[1]Department of Computer Science, City University of Hong Kong

[2]School of Mathematical Sciences, University of Science and Technology of China

[3]School of Computer Science and Engineering, Nanyang Technological University

{qijizhang3-c@my., jh.hou@, yueqian4-c@my.}cityu.edu.hk, juyong@ustc.edu.cn, yhe@ntu.edu.sg

Abstract

Although convolutional neural networks have achieved remarkable success in analyzing 2D images/videos, it is still non-trivial to apply the well-developed 2D techniques in regular domains to the irregular 3D point cloud data. To bridge this gap, we propose ParaNet, a novel end-to-end deep learning framework, for representing 3D point clouds in a completely regular and nearly lossless manner. To be specific, ParaNet converts an irregular 3D point cloud into a regular 2D color image, named point geometry image (PGI), where each pixel encodes the spatial coordinates of a point. In contrast to conventional regular representation modalities based on multi-view projection and voxelization, the proposed representation is differentiable and reversible. Technically, ParaNet is composed of a surface embedding module, which parameterizes 3D surface points onto a unit square, and a grid resampling module, which resamples the embedded 2D manifold over regular dense grids. Note that ParaNet is unsupervised, i.e., the training simply relies on reference-free geometry constraints. The PGIs can be seamlessly coupled with a task network established upon standard and mature techniques for 2D images/videos to realize a specific task for 3D point clouds. We evaluate ParaNet over shape classification and point cloud upsampling, in which our solutions perform favorably against the existing state-of-the-art methods. We believe such a paradigm will open up many possibilities to advance the progress of deep learning-based point cloud processing and understanding.

1. Introduction

The recent decade has witnessed remarkable success of deep convolutional neural networks (CNNs) in analyzing regular visual modalities such as 2D images/videos and 3D volumes [21, 17, 42, 48, 38, 30, 12, 43]. In the mean-
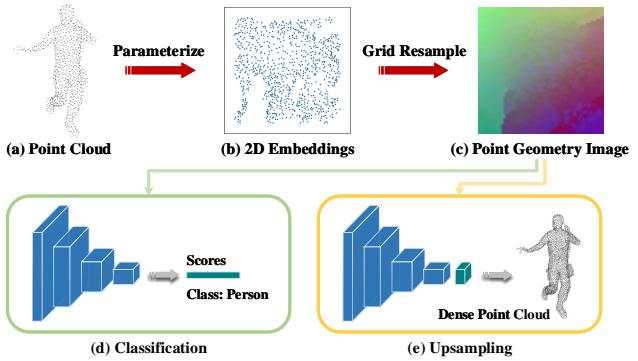

Figure 1. Illustration of the pipeline of ParaNet. ParaNet maps an input 3D point cloud (a) to a 2D domain (b) and adopts grid resampling to produce a 2D color image named point geometry image (PGI) (c), which is a complete regular structure that explicitly encodes 3D information into pixel colors and can faithfully represent the geometry of the input shape. Thanks to the regular structure, the generated geometry images enable the standard 2D CNNs for 3D applications, such as classification (d) and upsampling (e). Note that ParaNet is unsupervised, i.e., the ground-truth PGIs are not required during training.

time, with the advanced 3D sensing technology, 3D point clouds become a popular scheme for representing 3D objects and scenes and have been used in a wide range of applications, including immersive telepresence [34], 3D city reconstruction [22, 33], autonomous driving [4, 23], and virtual/augmented reality [13, 40]. However, due to the irregular and orderless nature of point clouds, applying the well-developed CNNs is highly non-trivial.

In order to apply the well-developed CNNs to irregular 3D point clouds, there are two main classes of approaches: rasterization-based methods and point-based methods. The former converts the input model into either a regular 3D volume via voxelization or a collection of multi-view 2D images using projection. Though one can directly apply the standard 2D/3D CNNs to the regularly rasterized data, their performances are limited by either irreversible information loss or high computational complexity. The latter
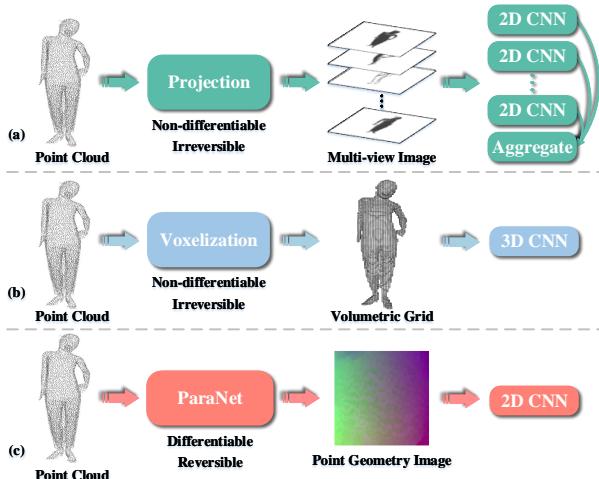
---

*Corresponding author.

1

Figure 2. Illustration of three classes of methods for applying the regular-data-fed CNNs to 3D point clouds. (a) Projection-based methods take 3D point clouds as a collection of multi-view images, and adopts multiple 2D CNNs with additional viewpoint aggregation. (b) Voxelization-based methods quantize point clouds as volumetric grids, which are processed by 3D CNNs. (c) ParaNet converts the input model into a PGI and adopts 2D CNNs.

takes 3D point clouds directly as input, and extracts features from each point. For example, the pioneering work, PointNet [35], can be viewed as 1×1 convolution applied to each point. Many follow-up works aim at designing convolution-like operators on point clouds for feature extraction [45, 14, 24, 49, 26, 54]. Each point-based convolution operator has its own merits and limitations. Currently, there is no unified framework adopted by the community. Moreover, it is observed that in point-based networks most of the computational resources are wasted on the process of neighborhood construction (e.g., k-NN) and structurization, not on the actual feature extraction.

Instead of seeking for convolution-like operators on unstructured points, we consider a different paradigm that converts an irregular 3D point cloud to a completely regular 2D representation where standard 2D CNNs can be applied. In the computer graphics community, there are extensive research on mesh parameterization. When mapping a 3D surface to a 2D domain, distortion is inevitable unless the surface is developable. Therefore, most of the existing techniques formulate parameterization as an optimization problem, aiming at finding a balance between distortion and parameterization quality (e.g., the number of singularities, continuity along cuts, etc). Although the state-of-the-art methods [3, 31] can compute globally smooth and seamless parameterization with low angle and area distortions, these approaches highly rely on the explicit connectivity information encoded in meshes, extending them to point clouds is highly non-trivial. Moreover, they usually work for shapes with simple geometry and topology, since the complexity

and difficulty in solving the optimization problem increases significantly with the complexity of geometry and topology.

In this paper we propose an end-to-end deep learning-based framework, called ParaNet, which is capable of transforming an arbitrary 3D point cloud into a completely regular 2D structure dubbed as point geometry image (PGI), which encodes the Cartesian coordinates of 3D points (x, y, z) as the color values of pixels (r, g, b). See Fig. 1. Since the generated PGIs can faithfully represent the input shape and naturally fit into the existing CNN pipelines, it bridges the gap between 3D geometry and the powerful deep learning techniques well-investigated for regular data structures. Technically, we design ParaNet as a two-stage network and train it in an end-to-end unsupervised fashion. In the first stage, the points of an input shape pass through a surface embedding module and are parameterized into a unit square while maintaining local proximity as much as possible. In the second stage, the grid resampling module converts the 2D samples to a PGI. The ParaNet can be seamlessly coupled with downstream task networks established upon standard convolution techniques to boost various point cloud applications such as classification and upsampling.

Summary of Contributions. ParaNet is the first end-to-end deep neural network for representing an irregular 3D point cloud as a regular 2D image amenable to conventional CNNs driven by the standard convolution. Compared with multi-view projection and voxelization based approaches [46, 16, 36, 55, 32, 39, 50, 19], our PGI-based representation modality is more accurate and maintains reversible, which means that the original point clouds can be directly restored without borrowing additional computations. Furthermore, as illustrated in Fig. 2, the generation process of PGI is differentiable and can be optimized by a deep learning framework, whereas rasterization-based methods adopt non-differentiable quantization. To validate its potential in point cloud analysis, we combine ParaNet with two downstream task networks, classification and patch-based upsampling, and obtain favorable performance compared with state-of-the-art methods. The proposed regular point cloud representation modality enables effortless adaptation of the mature visual processing techniques originally developed for 2D images/videos, making the wide range of 2D computational tools available to the point cloud community.

2. Related Work

2.1. Rasterization-based Point Cloud Analysis

View projection [46, 16, 36] generates a set of 2D images by setting virtual cameras around 3D shape. Although multi-view projection is able to utilize well-studied 2D CNN for feature extraction, it suffers from information loss [19] and is not easily extended for fine-grained 3D tasks

like segmentation [5]. Another rasterization-based scheme is to voxelize point clouds into quantized volumetric grids followed by standard 3D CNNs [55, 32, 39, 50, 19]. However, voxelization suffers from inaccurate data representation, or heavy computation and large memory expense, depending on the resolution.

2.2. Convolution on Point Clouds

To eliminate quantization loss, latest researches focus on designing deep learning based architectures directly operated on point clouds without any rasterization procedure as pre-processing. Qi *et al.* [35] developed the pioneering point-based deep set architecture, *i.e.*, PointNet, that employs shared multi-layer perceptrons for point-wise feature embedding and achieves permutation-invariance by max-pooling, which is improved in PointNet++ [37] by incorporating neighbor information to model local and global geometry hierarchically. Based on such point-wise feature learning, more methods [45, 14, 24, 49, 26, 54] were proposed with different design in local feature aggregations and hierarchical learning strategies. In general, existing studies devote to tailoring *convolution-like* operators and *CNN-like* architectures for point cloud feature extraction. Compared with rasterization-based methods, point-based methods does not have quantization issue and can achieve better performance. Unlike image analysis in which 2D CNNs are dominating, currently there is no standard framework for 3D point clouds. Moreover, directly processing irregular points is computationally expensive, due to extra resources for structurization and neighborhood construction [29].

2.3. Parameterization and Geometry Images

In digital geometry processing, parameterization is a typical way to convert an irregular representation (e.g., polygonal mesh, point clouds) to a regular one. Since a map from 3D surfaces to 2D domains inevitably has distortion unless the surface is developable, conformal parameterization is popular thanks to its angle preserving property [10]. It is well known that area distortion of a conformal parameterization is closely related to the singularities of parameterization, i.e., the number, their locations and indices. Modern approaches often formulate conformal parameterization as a mixed-integer programming [2], in which the locations of singularities are continuous, and their numbers and indices are discrete. Once the parameterization is computed, one can generate a multi-chart geometry image by partitioning the model via a motorcycle graph [3]. These methods are theoretically sound and elegant, however, they are not practical for surfaces with complex geometry and/or topology due to high computational cost. Moreover, these approaches work only for single-component manifold surfaces, whereas many man-made models are non-manifolds with multiple components. Note that the proposed point geometry images are fundamentally different from the classic geometry images in terms of generation and application.

2.4. Deformation-based 3D Shape Representation

FoldingNet, proposed by Yang *et al.* [57], is a novel deep auto-encoder. The folding-based decoder, which consists of shared multi-layer perceptrons, deforms a predefined 2D regular grid to the input 3D point cloud. The idea of deforming a predefined template in shape modeling is also adopted in many other works. For example, AtlasNet [8] achieves better reconstruction quality by deforming multiple 2D planes. Deprelle *et al.* [6] proposed to learn adaptive elementary structures that better fit the whole training data, and 3D-Coded [7] predicts correspondence for meshes via deforming the human template.

These methods demonstrate the ability for deep neural networks to deform one shape to another. However, existing works require either pre-defined or pre-generated templates (*e.g.*, a 2D grid with fixed resolution, a learned set of elementary structures, or a 3D triangle mesh with fixed connectivity) to reconstruct the input point cloud or mesh. In this paper, we show that the opposite direction, i.e., unfolding/deforming arbitrary 3D point clouds to 2D regular grids of arbitrary resolution, is also applicable, which has never been explored before.

3. Proposed Method

3.1. Overview

This work explores the potential to encode irregular 3D geometry in regular 2D grids and then apply conventional CNN architectures to perform specific point cloud processing tasks. Given a point cloud $\mathbf{P} \in \mathbb{R}^{N \times 3}$ with N 3D points $\mathbf{p}_i = (x_i, y_i, z_i)$, where $i = 1, 2, ..., N$, we construct a completely regular representation structure $\mathbf{G} \in \mathbb{R}^{m \times m \times 3}$, dubbed as a point geometry image (PGI), capturing the Cartesian coordinates of spatial points in the color channels of a 2D image. The generated PGI can be directly reshaped into a point cloud $\mathbf{Q} \in \mathbb{R}^{M \times 3}$, where $M = m \times m$. In practice, we always require $M > N$ so that the original points are redundantly represented in the PGI, reducing the loss of geometric information effectively.

The overall workflow of ParaNet is illustrated in Fig. 3. We start by extracting the global feature $\mathbf{c} \in \mathbb{R}^D$ from the input point cloud $\mathbf{P}$, and then generate a PGI in two stages. In the first stage, the surface embedding module maps each 3D spatial point to a 2D point over a unit square domain. In the second stage, the grid resampling module produces a regular point geometry image by either grid resampling or a differentiable relaxation of the nearest grid neighbor resampling. In our implementation, we employ the popular DGCNN [52] as the backbone point feature extractor.

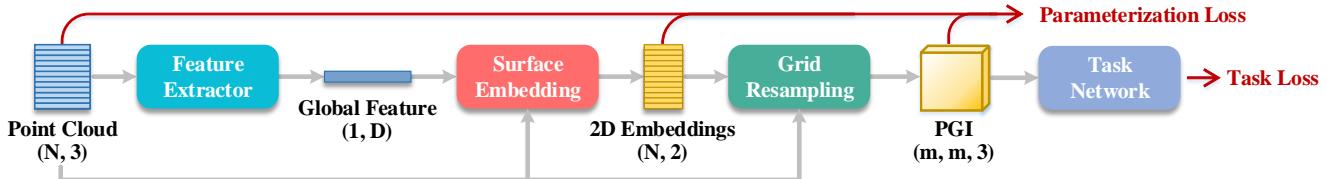Thanks to the regular structure, PGIs can be fed into the

Figure 3. ParaNet consists of feature extractor and two core modules, namely surface embedding and grid resampling. The feature extractor computes a global feature for the input 3D point cloud. Using the global feature, the surface unfolding module maps each 3D point to a unique 2D point in a square. Then the grid resampling module generates a geometry image, which can be fed into a CNN-based task network. The PGI generation is unsupervised and only regularized by geometric constraints denoted as the parameterization loss. It can also be jointly optimized with the specific task loss.
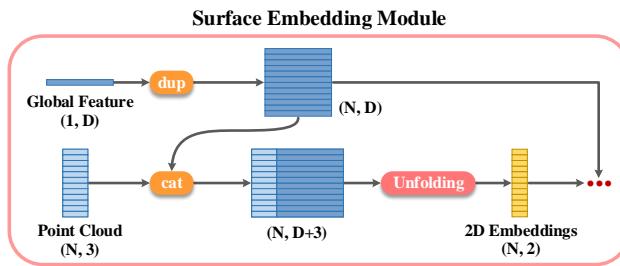

Figure 4. The surface embedding module assigns each 3D point $\mathbf{p}_i$ a unique pair of 2D coordinates (u_i, v_i), where $0 \leq u_i, v_i \leq 1$.

Figure 5. The unfold operators can be applied multiple times like function composition. (a) shows the input point cloud $\mathbf{P}$, and (b), (c) and (d) show the 2D embedded results of unfolding once, twice and three times, respectively.

subsequent CNN-based downstream task networks. In the paper, we demonstrate the potential of PGIs on classification (Sec. 4.2) and upsampling (Sec. 4.3). *Please refer to the Supplementary Material for the detailed discussions on the differences between our PGI and the classic GI representation.*

3.2. Surface Embedding Module

The surface embedding module applies the unfolding operator twice to map each 3D point to a unique location in a unit square. See Fig. 4. Specifically, we first duplicate the global feature N times and arrange them in a row-wise matrix $\mathbf{C} \in \mathbb{R}^{N \times D}$. Concatenating $\mathbf{C}$ with the input Cartesian coordinates $\mathbf{P}$, we obtain the initial embeddings $\mathbf{H}_1 \in \mathbb{R}^{N \times (D+3)}$. We then apply a four-layer perceptron to the rows of $\mathbf{H}_1$ to generate intermediate 2D embeddings $\mathbf{E}_1 \in \mathbb{R}^{N \times 2}$.

We apply the second unfolding operator in a similar fashion: we concatenate $\mathbf{E}_1$ with $\mathbf{C}$ to form $\mathbf{H}_2 \in \mathbb{R}^{N \times (D+2)}$, and then feed $\mathbf{H}_2$ into another four-layer perceptron yields the final 2D embeddings $\mathbf{E} \in \mathbb{R}^{N \times 2}$.

Putting it all together, we can express the surface embedding procedure as

$$\mathbf{E} = \sigma(f_2([f_1([\mathbf{P}; \mathbf{C}]); \mathbf{C}])), \tag{1}$$

where $[\cdot; \cdot]$ denotes channel-wise concatenation between two feature matrices, $f_1(\cdot)$ and $f_2(\cdot)$ are two separate unfolding units, and σ is the sigmoid activation function to
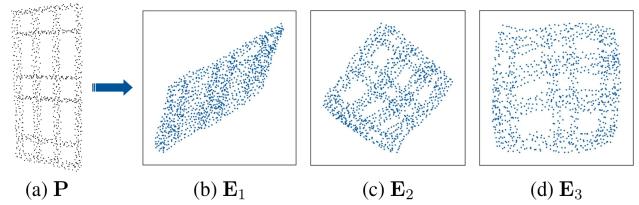
normalize the embedded 2D points in the range of $[0, 1]$. The 2D embeddings after various unfold operators are visualized in Fig. 5. We observe that two-time unfolding leads to satisfactory results.

For convenience, we denote the i-th point contained in $\mathbf{E}$ as $\mathbf{e}_i = (u_i, v_i)$. It is worth mentioning that there exist one-to-one correspondence between the input point cloud $\mathbf{P}$ and the 2D embeddings $\mathbf{E}$, i.e., each 3D point $\mathbf{p}_i \in \mathbb{R}^3$ is mapped to a unique 2D position $\mathbf{e}_i \in \mathbb{R}^2$.

To prevent the embedded 2D points $\mathbf{e}_i$ from being highly clustered, we design a simple repulsion loss to stretch the point distribution by imposing punishment on clustered points until they are separated by a distance threshold T. Mathematically, we formulate the repulsion loss $\ell_{rep}(\cdot)$ for every point $\mathbf{e}_i$ as

$$\ell_{rep}(\mathbf{e}_i) = \begin{cases} 0, & \text{if } d_i \geq T \\ -\log(d_i + 1 - T), & \text{otherwise,} \end{cases} \tag{2}$$
$$\text{where } d_i = \min_{\mathbf{e}_j \in \mathbf{E} \setminus \{\mathbf{e}_i\}} \|\mathbf{e}_i - \mathbf{e}_j\|_2.$$

In our implementation we empirically set the distance threshold $T = \frac{1}{m-1}$.

We define the objective function for the surface embedding module as:

$$\mathcal{L}_{rep} = \frac{1}{N} \sum_{i=1}^{N} \ell_{rep}(\mathbf{e}_i). \tag{3}$$

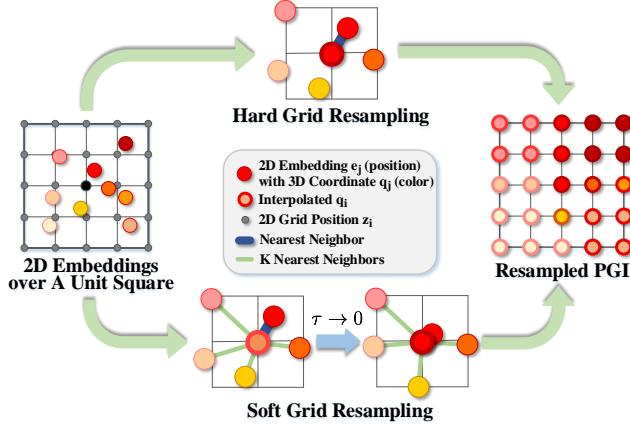We observe that by minimizing $\mathcal{L}_{rep}$, the surface embed-

Figure 6. The grid resampling module converts 2D parameters $\{(u_i, v_i)\}_{i=1}^N$ to an $m \times m$ geometry image. It supports both hard and soft resampling. The former maps each 2D sample to the nearest grid point and the latter adopts distance-weighted interpolation to assign the values for grid points.

ding module is capable of unfolding 3D surfaces onto a unit square. However, the embedded 2D points are not likely on the grid positions of the regular image lattice. Therefore, we need a resampling module (Sec. 3.3) to produce a regular geometry image.

3.3. Grid Resampling Module

The grid resampling module consumes the irregularly-arranged 2D embeddings $\mathbf{E} \in \mathbb{R}^{N \times 2}$ and produces a regular PGI $\mathbf{G} \in \mathbb{R}^{m \times m \times 3}$ where m is the user-specified resolution.

There are two common strategies in resampling, as shown in Fig 6. One is to drag each 2D sample $\mathbf{e}_i$ to the nearest pixel, and the other is to compute the pixel value using bilinear interpolation. Here, we denote the two strategies as hard grid resampling and soft grid resampling, respectively.

Hard Grid Resampling. We start by constructing a canonical 2D grid uniformly defined on a unit square domain, denoted as $\mathbf{Z} \in \mathbb{R}^{M \times 2}$ containing M points. Each row of matrix $\mathbf{Z}$ corresponds to a certain 2D point $\mathbf{z}_i$ within an $m \times m$ gridding structure. Suppose that, in the point set $\mathbf{E}$, the nearest neighbor of $\mathbf{z}_i$ is $\mathbf{e}_j$. Based on the exact row-wise matching relations between $\mathbf{P}$ and $\mathbf{E}$, we can deduce a 2D array $\mathbf{Q} \in \mathbb{R}^{M \times 3}$ whose i-th entry $\mathbf{q}_i \in \mathbb{R}^3$ is the j-th entry of $\mathbf{P}$. We formulate the hard resampling as follows:

$$\mathbf{q}_i = \mathbf{p}_{j^*}, \text{ where } j^* = \underset{j \in \{1, 2, \cdots, N\}}{\arg\min} \|\mathbf{z}_i - \mathbf{e}_j\|_2. \quad (4)$$

After that, we reshape the $M \times 3$ array $\mathbf{Q}$ into an $m \times m \times 3$ PGI $\mathbf{G}$. As two mapped samples $\mathbf{e}_i$ and $\mathbf{e}_j$ could be cluttered, there is a possibility that some 3D points are not included in $\mathbf{G}$. This problem can be reduced by increasing

the PGI resolution m. With a sufficiently high resolution, PGI is guaranteed to include all points of the input point cloud, resulting a lossless representation.

Soft Grid Resampling. Notice that the hard grid resampling workflow is non-differentiable, which hinders end-to-end optimization. To overcome this limitation, we further provide an annealing strategy to produce PGIs in a differentiable manner. In soft resampling, we model $\mathbf{q}_i$ as a weighted average of the input points $\mathbf{P}$. For grid point $\mathbf{z}_i$, we select its K nearest neighbors from $\mathbf{E}$, which are denoted as $\{\mathbf{e}_k\}_{k=1}^K$, and their corresponding 3D points $\{\mathbf{p}_k\}_{k=1}^K$. We then determine a set of weights using the distances between $\mathbf{z}_i$ and its K neighbors:

$$\varpi_{ik} = \frac{\exp(-d_{ik}/|\tau|)}{\sum_{j=1}^K \exp(-d_{ij}/|\tau|)}, \quad (5)$$

where $d_{ik} = \|\mathbf{z}_i - \mathbf{e}_k\|_2$, and τ is a temperature coefficient. We express the i-th entry of $\mathbf{Q}$ as

$$\mathbf{q}_i = \sum_{k=1}^K \varpi_{ik} \mathbf{p}_k. \quad (6)$$

During annealing, the distribution of weights gradually converges to the Kronecker delta function with $\tau \to 0$, approximating the nearest neighbor point. We can easily achieve this by adding a parameter regularization term:

$$\mathcal{L}_{ann} = |\tau| \quad (7)$$

Combining Eq. (3) and Eq. (7), we obtain the objective function for the unsupervised ParaNet:

$$\mathcal{L}_{para} = \alpha \mathcal{L}_{rep} + \beta \mathcal{L}_{ann}. \quad (8)$$

Note that annealing is dropped in hard grid resampling.

Fig. 7 shows some visual examples by running ParaNet over input shapes after sufficient iterations. We can observe that the PGIs accurately represent the original point clouds while maintaining satisfactory smoothness.

4. Experimental Results

4.1. Training Strategies

As an unsupervised learning approach, ParaNet enables flexible and customized optimization schemes. In order to fit the specific characteristics and requirements of different application scenarios, we investigated three types of training strategies: 1) joint optimization; 2) offline independent optimization; and 3) online independent optimization. Note that we employ soft grid resampling for joint optimization, and hard grid resampling for independent optimization.

Joint Optimization (JO). ParaNet and the downstream task network are jointly trained with a combined objective
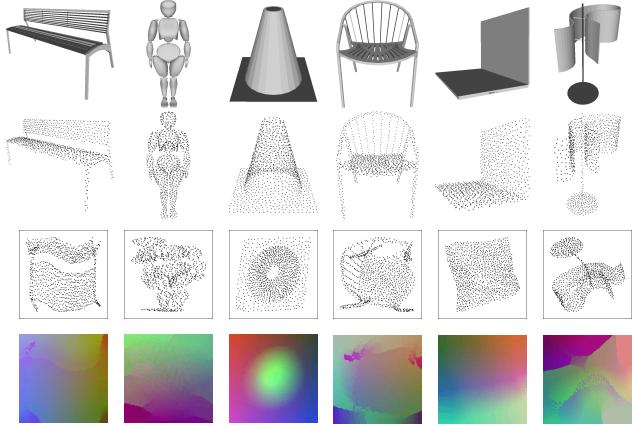
Figure 7. PGI results. Row 1: 3D meshes. Row 2: Point clouds $\mathbf{P}$. Row 3: 2D embedded results $\mathbf{E}_2$. Row 4: Point geometry images of resolution 128×128. From left to right, the Chamfer distance errors (10^{-8}) are 1.71, 1.28, 1.89, 1.04, 1.72 and 1.78 respectively. See *Supplementary Material* for more results.

function involving the parameterization loss $\mathcal{L}_{para}$ and the task-specific loss $\mathcal{L}_{task}$. We pre-train the ParaNet before connecting it with the task network to stabilize and speed up the joint training process. The JO strategy benefits from the task-oriented learning paradigm. Thanks to the implicit guidance of the task network, the generated PGIs can be automatically adjusted to suit downstream applications.

Offline Independent Optimization (Off-IO). We start by pre-training ParaNet on the whole training set, and then freeze its parameters before connecting it with the downstream task network. Accordingly, we only exploit the task-specific loss $\mathcal{L}_{task}$ to supervise the overall framework. We observe that the independent optimization strategy usually leads to PGIs with higher representation accuracy, while sacrificing the possibility of adaptively adjusting the geometry parameterization process.

Online Independent Optimization (On-IO). We separately optimize ParaNet for every input shape with adequate iterations to obtain a nearly lossless representation during both training and testing. We can achieve this by generating an accurate PGI for every single input shape over the training and testing sets. The generated PGIs are cached and further fed into the downstream task network. Obviously, the On-IO strategy is much slower than the offline strategy, but it produces highly-precise representation of input point clouds with little information loss. In practice, On-IO can be greatly accelerated by feeding batch-wise inputs.

4.2. Shape Classification

Task network. Image classification has been adequately addressed in numerous CNN-based architectures. In our shape classification task, we adopted the commonly-used
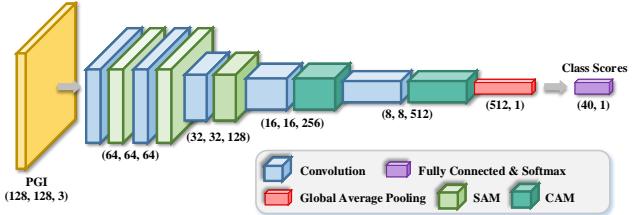

Figure 8. ParaNet fed into a classification network.

Table 1. Classification accuracy on ModelNet40.

Method	Input	Accuracy (%)
VoxNet [32]	voxels	85.9
KD-Net [19]	1024 points	91.8
PointNet [35]	1024 points	89.2
PointNet++ [37]	5000 points + normal	91.9
3D-GCN [27]	1024 points	92.1
SpiderCNN [56]	1024 points + normal	92.4
PointConv [54]	1024 points + normal	92.5
A-CNN [20]	1024 points	92.6
KPConv [47]	6800 points	92.9
DGCNN [52]	1024 points	92.9
ParaNet-SC (JO)	1024 points	**93.1**
ParaNet-SC (Off-IO)	1024 points	92.7
ParaNet-SC (On-IO)	1024 points	92.9

ResNet-18 [12] architecture, which consists of five convolution layers, as illustrated in Fig. 8. Considering that the original point cloud is redundantly represented in the PGI, we applied three spatial attention modules (SAM) to highlight informative regions, and another two channel attention modules (CAM) were equipped to boost feature learning. Afterwards, the extracted feature maps were squeezed into a one-dimensional feature vector by global average pooling, and passed through a fully-connected layer followed by Softmax to predict the class probabilities. We employed cross-entropy as the task loss to supervise the task network. Notice that we did not utilize the ImageNet [21] pretrained parameters for fair comparisons.

Development protocols. We evaluated the shape classification performance of our framework over the ModelNet40 [55] benchmark dataset, which contains 12311 CAD models from 40 man-made object categories. Following the official train-test partition, we employed 9843 shapes for training and the rest 2468 for testing. We used Poisson Disk Sampling to generate 1024 points from the original mesh. Common data augmentation techniques including random point dropout and jittering point positions by Gaussian noises were employed to enrich the training data and boost the generalization ability of the learning model. For parameters in Eq. 8, we empirically set the parameters

$\alpha = 1$ and $\beta = 0.1$.

Comparison with state-of-the-art methods. We report the performances of the proposed framework under different training strategies in Table 1, which includes 10 classic and latest state-of-the-art competitors for comparisons. As shown in Table 1, our ParaNet model under the JO strategy achieves the highest classification accuracy compared with other rasterization- and point-based frameworks. An interesting observation is that, although the Off-IO and On-IO schemes typically produce more accurate PGI representations, the JO scheme shows superiority benefiting from the end-to-end task-oriented learning paradigm.

Ablation studies. We conducted ablation studies to explore the effectiveness and potential of the proposed PGI representation. The results of different model variants of the ParaNet-JO are reported in Table 2. To demonstrate the necessity of representing raw point clouds as PGIs, we removed the ParaNet from the full pipeline and directly and randomly reshape the input point cloud from a 2D array to the form of a color image, denoted as ParaNet-SC-random. Under this circumstance, the performance significantly drops from 93.1% to 45.6%, which reveals that it is non-trivial to apply standard convolutions to process irregular and unstructured point clouds. Then, we designed a naive baseline CNN architecture serving as the downstream task network to form the method ParaNet-SC-baseline. Details of the baseline design can be found in the *Supplemental Material*. This simple variant also achieves favorable performance of 91.9%. When we replaced the backbone network in the baseline with a more powerful ResNet18 [12] encoder, the classification accuracy for ParaNet-SC-ResNet18 increases to 92.6%. Moreover, we explored whether the success of image attention mechanisms can be extended to our task setting. Empirically, we observe performance decrease when the SAM or the CAM modules are removed from the full pipeline, which implies that our method enables direct adaptation of existing visual techniques that have been proven to be effective in image domain applications. We can expect to achieve further performance gains as more advanced 2D techniques are introduced to cooperate with ParaNet.

We further explored the impact of generating the PGIs with different resolutions. As discussed before, the original point cloud is redundantly represented in image pixels. Predictably, the information loss will decrease as the image resolution increases. Thus, we are able to flexibly adjust the representation accuracy at the cost of the representation redundancy. As reported in Table 3, low resolution of the parameterized PGI leads to degraded performance, since a noticeable number of points may be lost during grid resampling. When the image resolution is sufficiently large to accurately represent the point cloud, the performance gain vanishes accordingly.

Table 2. Quantitative comparisons among different variants under the JO strategy over the ModelNet40 dataset.

Method	Accuracy (%)
ParaNet-SC-random	45.6
ParaNet-SC-baseline	91.9
ParaNet-SC-ResNet18	92.6
ParaNet-SC *w/o* CAM	92.8
ParaNet-SC *w/o* SAM	93.0
ParaNet-SC (full)	**93.1**

Table 3. Impacts of different resolution of PGIs.

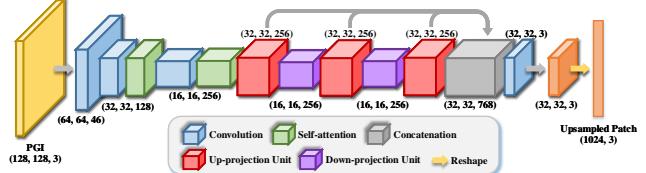| Resolution	Accuracy (%)	CD Errors
32×32	91.6	1.14×10^{-3}
48×48	92.5	2.12×10^{-4}
64×64	93.0	4.49×10^{-5}
96×96	**93.1**	7.38×10^{-6}
128×128	**93.1**	$\mathbf{2.32 \times 10^{-6}}$

Figure 9. ParaNet fed into a upsampling network.

4.3. Point Cloud Upsampling

Task network. Extensive studies have been conducted for image super-resolution, which provide valuable insights for point cloud upsampling. We followed the common patch-based processing pipeline [25] to achieve $4\times$ upsampling for non-uniform inputs. As illustrated in Fig. 9, we first converted input patches into PGIs, which passed through the subsequent convolutional layers for feature embedding. The back projection mechanism [11] was introduced to fully exploit the mutual dependencies of low- and high-resolution contents, and self-attention operations [51] were introduced to encode global prior of the input patch. We utilized the Earth Mover's Distance (EMD) to supervise point cloud generation, and employed a uniformity constraint to enhance point distribution. Different from shape classification, the upsampling task requires highly-accurate representations with little information loss. Therefore, we employed the On-IO scheme for training.

Development protocols. Following previous study [25], we collected 147 3D mesh models from the released datasets of PU-Net [59] and MPU [58] as well as Visionair
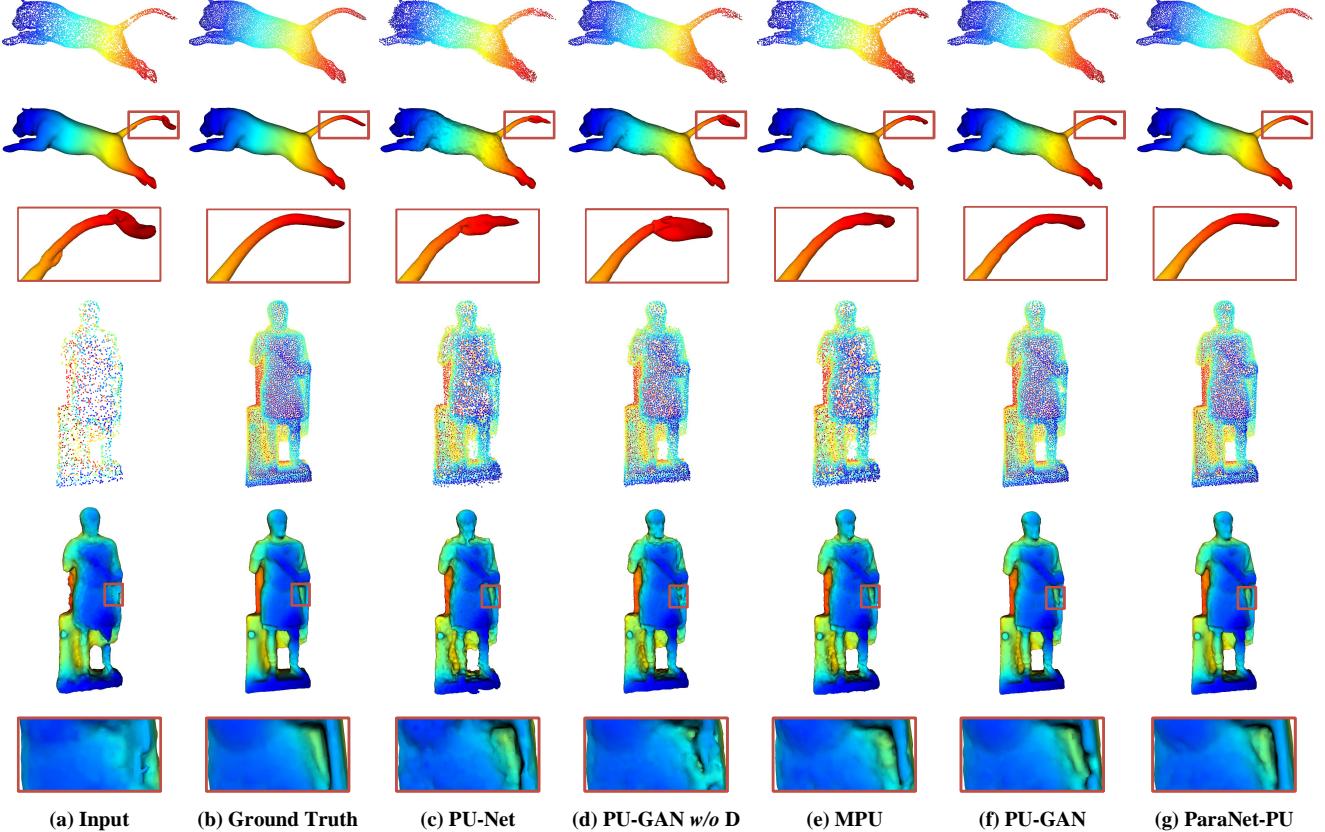
Figure 10. Point cloud upsampling with a factor $4\times$. To ease checking the result quality, we show the triangle meshes reconstructed from the upsampled point clouds. See *Supplementary Material* for more results.

repository [1], among which 120 for training and 27 for testing. We used Poisson disk sampling to sample 8192 points as ground-truths, and randomly selected 2048 points as inputs. The size of extracted patches is 256, and the resolution of converted PGIs is 128×128. We employed three evaluation metrics: 1) point-to-surface (P2F) distance, 2) Chamfer distance (CD), and 3) Hausdorff distance (HD).

Comparison with state-of-the-art methods. We compared our pipeline, *i.e.*, ParaNet-PU, with three deep point upsampling models by retraining their models on our dataset. Note that PU-GAN [25] additionally adopts adversarial learning, hence, we also report the performance of its point generator, *i.e.*, PU-GAN *w/o* D. As reported in Table 4, our PGI-driven framework outperforms these point-based architectures. We provided some visual comparisons of upsampled point clouds and the reconstructed surfaces using [18] in Fig. 10, from which we can observe that our results better restore detailed shape geometry and contain less noises that deviating from the underlying surface.

Table 4. Quantitative comparison of different methods for $4\times$ point cloud upsampling. The best results are highlighted in bold.

Method	P2F (10^{-3})	CD (10^{-3})	HD (10^{-3})
PU-Net [59]	6.97	0.72	8.93
PU-GAN *w/o D* [25]	4.75	0.59	7.44
MPU [58]	3.93	0.49	6.06
PU-GAN [25]	2.40	0.29	4.75
ParaNet-PU	**2.26**	**0.28**	**4.44**

5. Conclusion

We proposed an end-to-end deep neural network, *i.e.*, ParaNet, to convert irregular 3D point clouds into a completely regular 2D representation modality, which is an ideal input of standard 2D convolutional neural networks. ParaNet can be trained either in an unsupervised manner or jointly with the specific downstream task network. We demonstrated the effectiveness of ParaNet on shape classification and point cloud upsampling. Extensive experiments

demonstrate the superiority of our point cloud processing pipelines. Our method naturally bridges the gap between 2D CNNs and 3D point cloud processing. We believe it will open a door to apply well-developed 2D deep learning tools to 3D applications. In future studies, we would like to explore richer applications based on point geometry image for point cloud analysis.

References

[1] Visionair. http://www.infra-visionair.eu/, 2019-07. 8

[2] David Bommes, Henrik Zimmer, and Leif Kobbelt. Mixed-integer quadrangulation. *ACM Trans. Graph.*, 28(3):77, 2009. 3, 12

[3] Marcel Campen, David Bommes, and Leif Kobbelt. Quantized global parametrization. *ACM Trans. Graph.*, 34(6):192:1–192:12, 2015. 2, 3

[4] Xiaozhi Chen, Huimin Ma, Ji Wan, Bo Li, and Tian Xia. Multi-view 3d object detection network for autonomous driving. In *Proceedings of the IEEE Conference on Computer Vision and Pattern Recognition*, pages 1907–1915, 2017. 1

[5] Angela Dai, Angel X Chang, Manolis Savva, Maciej Halber, Thomas Funkhouser, and Matthias Nießner. Scannet: Richly-annotated 3d reconstructions of indoor scenes. In *Proceedings of the IEEE Conference on Computer Vision and Pattern Recognition*, pages 5828–5839, 2017. 3

[6] Theo Deprelle, Thibault Groueix, Matthew Fisher, Vladimir Kim, Bryan Russell, and Mathieu Aubry. Learning elementary structures for 3d shape generation and matching. In *Advances in Neural Information Processing Systems*, pages 7435–7445, 2019. 3

[7] Thibault Groueix, Matthew Fisher, Vladimir G Kim, Bryan C Russell, and Mathieu Aubry. 3d-coded: 3d correspondences by deep deformation. In *Proceedings of the European Conference on Computer Vision (ECCV)*, pages 230–246, 2018. 3

[8] Thibault Groueix, Matthew Fisher, Vladimir G Kim, Bryan C Russell, and Mathieu Aubry. A papier-mâché approach to learning 3d surface generation. In *Proceedings of the IEEE conference on computer vision and pattern recognition*, pages 216–224, 2018. 3

[9] Xianfeng Gu, Steven J. Gortler, and Hugues Hoppe. Geometry images. In *Proceedings of the 29th Annual Conference on Computer Graphics and Interactive Techniques*, pages 355–361, 2002. 12

[10] Xianfeng Gu and Shing-Tung Yau. Global conformal parameterization. In Leif Kobbelt, Peter Schröder, and Hugues Hoppe, editors, *First Eurographics Symposium on Geometry Processing*, volume 43, pages 127–137, 2003. 3

[11] Muhammad Haris, Gregory Shakhnarovich, and Norimichi Ukita. Deep back-projection networks for super-resolution. In *Proceedings of the IEEE conference on computer vision and pattern recognition*, pages 1664–1673, 2018. 7, 15

[12] Kaiming He, Xiangyu Zhang, Shaoqing Ren, and Jian Sun. Deep residual learning for image recognition. In *Proceedings of the IEEE conference on computer vision and pattern recognition*, pages 770–778, 2016. 1, 6, 7, 12

[13] Robert Held, Ankit Gupta, Brian Curless, and Maneesh Agrawala. 3d puppetry: a kinect-based interface for 3d animation. In *UIST*, pages 423–434. Citeseer, 2012. 1

[14] Varun Jampani, Martin Kiefel, and Peter V Gehler. Learning sparse high dimensional filters: Image filtering, dense crfs and bilateral neural networks. In *Proceedings of the IEEE Conference on Computer Vision and Pattern Recognition*, pages 4452–4461, 2016. 2, 3

[15] Miao Jin, Junho Kim, Feng Luo, and Xianfeng Gu. Discrete surface ricci flow. *IEEE Trans. Vis. Comput. Graph.*, 14(5):1030–1043, 2008. 12

[16] Evangelos Kalogerakis, Melinos Averkiou, Subhransu Maji, and Siddhartha Chaudhuri. 3d shape segmentation with projective convolutional networks. In *proceedings of the IEEE conference on computer vision and pattern recognition*, pages 3779–3788, 2017. 2

[17] Andrej Karpathy, George Toderici, Sanketh Shetty, Thomas Leung, Rahul Sukthankar, and Li Fei-Fei. Large-scale video classification with convolutional neural networks. In *Proceedings of the IEEE conference on Computer Vision and Pattern Recognition*, pages 1725–1732, 2014. 1

[18] Michael Kazhdan and Hugues Hoppe. Screened poisson surface reconstruction. *ACM Transactions on Graphics (ToG)*, 32(3):1–13, 2013. 8

[19] Roman Klokov and Victor Lempitsky. Escape from cells: Deep kd-networks for the recognition of 3d point cloud models. In *Proceedings of the IEEE International Conference on Computer Vision*, pages 863–872, 2017. 2, 3, 6

[20] Artem Komarichev, Zichun Zhong, and Jing Hua. A-cnn: Annularly convolutional neural networks on point clouds. In *Proceedings of the IEEE Conference on Computer Vision and Pattern Recognition*, pages 7421–7430, 2019. 6

[21] Alex Krizhevsky, Ilya Sutskever, and Geoffrey E Hinton. Imagenet classification with deep convolutional neural networks. In *Advances in neural information processing systems*, pages 1097–1105, 2012. 1, 6

[22] Florent Lafarge and Clément Mallet. Creating large-scale city models from 3d-point clouds: a robust approach with hybrid representation. *International Journal of Computer Vision*, 99(1):69–85, 2012. 1

[23] Bo Li. 3d fully convolutional network for vehicle detection in point cloud. In *2017 IEEE/RSJ International Conference on Intelligent Robots and Systems (IROS)*, pages 1513–1518. IEEE, 2017. 1

[24] Jiaxin Li, Ben M Chen, and Gim Hee Lee. So-net: Self-organizing network for point cloud analysis. In *Proceedings of the IEEE conference on computer vision and pattern recognition*, pages 9397–9406, 2018. 2, 3

[25] Ruihui Li, Xianzhi Li, Chi-Wing Fu, Daniel Cohen-Or, and Pheng-Ann Heng. Pu-gan: a point cloud upsampling adversarial network. In *Proceedings of the IEEE International Conference on Computer Vision*, pages 7203–7212, 2019. 7, 8

[26] Yangyan Li, Rui Bu, Mingchao Sun, Wei Wu, Xinhan Di, and Baoquan Chen. Pointcnn: Convolution on x-transformed points. In *Advances in neural information processing systems*, pages 820–830, 2018. 2, 3

[27] Zhi-Hao Lin, Sheng-Yu Huang, and Yu-Chiang Frank Wang. Convolution in the cloud: Learning deformable kernels in 3d graph convolution networks for point cloud analysis. In *Proceedings of the IEEE/CVF Conference on Computer Vision and Pattern Recognition*, pages 1800–1809, 2020. 6

[28] Ligang Liu, Lei Zhang, Yin Xu, Craig Gotsman, and Steven J. Gortler. A local/global approach to mesh parameterization. *Comput. Graph. Forum*, 27(5):1495–1504, 2008. 12

[29] Zhijian Liu, Haotian Tang, Yujun Lin, and Song Han. Point-voxel cnn for efficient 3d deep learning. In *Advances in Neural Information Processing Systems*, pages 965–975, 2019. 3

[30] Jonathan Long, Evan Shelhamer, and Trevor Darrell. Fully convolutional networks for semantic segmentation. In *Proceedings of the IEEE conference on computer vision and pattern recognition*, pages 3431–3440, 2015. 1

[31] Max Lyon, Marcel Campen, David Bommes, and Leif Kobbelt. Parametrization quantization with free boundaries for trimmed quad meshing. *ACM Trans. Graph.*, 38(4):51:1–51:14, 2019. 2

[32] Daniel Maturana and Sebastian Scherer. Voxnet: A 3d convolutional neural network for real-time object recognition. In *2015 IEEE/RSJ International Conference on Intelligent Robots and Systems (IROS)*, pages 922–928, 2015. 2, 3, 6

[33] Przemyslaw Musialski, Peter Wonka, Daniel G Aliaga, Michael Wimmer, Luc Van Gool, and Werner Purgathofer. A survey of urban reconstruction. In *Computer Graphics Forum*, volume 32, pages 146–177. Wiley Online Library, 2013. 1

[34] Sergio Orts-Escolano, Christoph Rhemann, Sean Fanello, Wayne Chang, Adarsh Kowdle, Yury Degtyarev, David Kim, Philip L Davidson, Sameh Khamis, Mingsong Dou, et al. Holoportation: Virtual 3d teleportation in real-time. In *Proceedings of the 29th Annual Symposium on User Interface Software and Technology*, pages 741–754. ACM, 2016. 1

[35] Charles R Qi, Hao Su, Kaichun Mo, and Leonidas J Guibas. Pointnet: Deep learning on point sets for 3d classification and segmentation. In *Proceedings of the IEEE conference on computer vision and pattern recognition*, pages 652–660, 2017. 2, 3, 6, 16

[36] Charles R Qi, Hao Su, Matthias Nießner, Angela Dai, Mengyuan Yan, and Leonidas J Guibas. Volumetric and multi-view cnns for object classification on 3d data. In *Proceedings of the IEEE conference on computer vision and pattern recognition*, pages 5648–5656, 2016. 2

[37] Charles Ruizhongtai Qi, Li Yi, Hao Su, and Leonidas J Guibas. Pointnet++: Deep hierarchical feature learning on point sets in a metric space. In *Advances in neural information processing systems*, pages 5099–5108, 2017. 3, 6

[38] Shaoqing Ren, Kaiming He, Ross Girshick, and Jian Sun. Faster r-cnn: Towards real-time object detection with region proposal networks. In *Advances in neural information processing systems*, pages 91–99, 2015. 1

[39] Gernot Riegler, Ali Osman Ulusoy, and Andreas Geiger. Octnet: Learning deep 3d representations at high resolutions. In *Proceedings of the IEEE Conference on Computer Vision and Pattern Recognition*, pages 3577–3586, 2017. 2, 3

[40] José Miguel Santana, Jochen Wendel, Agustín Trujillo, José Pablo Suárez, Alexander Simons, and Andreas Koch. Multimodal location based services—semantic 3d city data as virtual and augmented reality. In *Progress in Location-based Services 2016*, pages 329–353. Springer, 2017. 1

[41] Alla Sheffer, Bruno Lévy, Maxim Mogilnitsky, and Alexander Bogomyakov. ABF++: fast and robust angle based flattening. *ACM Trans. Graph.*, 24(2):311–330, 2005. 12

[42] Karen Simonyan and Andrew Zisserman. Two-stream convolutional networks for action recognition in videos. In *Advances in neural information processing systems*, pages 568–576, 2014. 1

[43] Shuran Song, Fisher Yu, Andy Zeng, Angel X Chang, Manolis Savva, and Thomas Funkhouser. Semantic scene completion from a single depth image. In *Proceedings of the IEEE Conference on Computer Vision and Pattern Recognition*, pages 1746–1754, 2017. 1

[44] Boris Springborn, Peter Schröder, and Ulrich Pinkall. Conformal equivalence of triangle meshes. *ACM Trans. Graph.*, 27(3):77, 2008. 12

[45] Hang Su, Varun Jampani, Deqing Sun, Subhransu Maji, Evangelos Kalogerakis, Ming-Hsuan Yang, and Jan Kautz. Splatnet: Sparse lattice networks for point cloud processing. In *Proceedings of the IEEE Conference on Computer Vision and Pattern Recognition*, pages 2530–2539, 2018. 2, 3

[46] Hang Su, Subhransu Maji, Evangelos Kalogerakis, and Erik Learned-Miller. Multi-view convolutional neural networks for 3d shape recognition. In *Proceedings of the IEEE International Conference on Computer Vision (ICCV)*, pages 945–953, 2015. 2

[47] Hugues Thomas, Charles R Qi, Jean-Emmanuel Deschaud, Beatriz Marcotegui, François Goulette, and Leonidas J Guibas. Kpconv: Flexible and deformable convolution for point clouds. In *Proceedings of the IEEE International Conference on Computer Vision*, pages 6411–6420, 2019. 6

[48] Du Tran, Lubomir Bourdev, Rob Fergus, Lorenzo Torresani, and Manohar Paluri. Learning spatiotemporal features with 3d convolutional networks. In *Proceedings of the IEEE international conference on computer vision*, pages 4489–4497, 2015. 1

[49] Nitika Verma, Edmond Boyer, and Jakob Verbeek. Feastnet: Feature-steered graph convolutions for 3d shape analysis. In *Proceedings of the IEEE conference on computer vision and pattern recognition*, pages 2598–2606, 2018. 2, 3

[50] Peng-Shuai Wang, Yang Liu, Yu-Xiao Guo, Chun-Yu Sun, and Xin Tong. O-cnn: Octree-based convolutional neural networks for 3d shape analysis. *ACM Transactions on Graphics (TOG)*, 36(4):1–11, 2017. 2, 3

[51] Xiaolong Wang, Ross Girshick, Abhinav Gupta, and Kaiming He. Non-local neural networks. In *Proceedings of the IEEE conference on computer vision and pattern recognition*, pages 7794–7803, 2018. 7, 15

[52] Yue Wang, Yongbin Sun, Ziwei Liu, Sanjay E Sarma, Michael M Bronstein, and Justin M Solomon. Dynamic graph cnn for learning on point clouds. *Acm Transactions On Graphics (tog)*, 38(5):1–12, 2019. 3, 6, 12, 16

[53] Sanghyun Woo, Jongchan Park, Joon-Young Lee, and In So Kweon. Cbam: Convolutional block attention module. In *Proceedings of the European conference on computer vision (ECCV)*, pages 3–19, 2018. 12, 13

[54] Wenxuan Wu, Zhongang Qi, and Li Fuxin. Pointconv: Deep convolutional networks on 3d point clouds. In *Proceedings of the IEEE Conference on Computer Vision and Pattern Recognition*, pages 9621–9630, 2019. 2, 3, 6

[55] Zhirong Wu, Shuran Song, Aditya Khosla, Fisher Yu, Linguang Zhang, Xiaoou Tang, and Jianxiong Xiao. 3d shapenets: A deep representation for volumetric shapes. In *Proceedings of the IEEE conference on computer vision and pattern recognition*, pages 1912–1920, 2015. 2, 3, 6, 12

[56] Yifan Xu, Tianqi Fan, Mingye Xu, Long Zeng, and Yu Qiao. Spidercnn: Deep learning on point sets with parameterized convolutional filters. In *Proceedings of the European Conference on Computer Vision (ECCV)*, pages 87–102, 2018. 6

[57] Yaoqing Yang, Chen Feng, Yiru Shen, and Dong Tian. Foldingnet: Point cloud auto-encoder via deep grid deformation. In *Proceedings of the IEEE Conference on Computer Vision and Pattern Recognition*, pages 206–215, 2018. 3

[58] Wang Yifan, Shihao Wu, Hui Huang, Daniel Cohen-Or, and Olga Sorkine-Hornung. Patch-based progressive 3d point set upsampling. In *Proceedings of the IEEE Conference on Computer Vision and Pattern Recognition*, pages 5958–5967, 2019. 7, 8

[59] Lequan Yu, Xianzhi Li, Chi-Wing Fu, Daniel Cohen-Or, and Pheng-Ann Heng. Pu-net: Point cloud upsampling network. In *Proceedings of the IEEE Conference on Computer Vision and Pattern Recognition*, pages 2790–2799, 2018. 7, 8, 15

[60] Hui Zhao, Kehua Su, Chenchen Li, Boyu Zhang, Lei Yang, Na Lei, Xiaoling Wang, Steven J. Gortler, and Xianfeng Gu. Mesh parametrization driven by unit normal flow. *Comput. Graph. Forum*, 39(1):34–49, 2020. 12

11

Supplementary Materials

1. Differences Between the Proposed PGIs and the Classic GIs

Both the proposed point geometry images (PGIs) and the classic geometry images (GIs) [9] are able to represent 3D shapes with a completely regular structure, *i.e.*, a color image. When the image resolution is sufficiently high, both can encode 3D geometry in a nearly lossless manner. Besides the above two common characteristics, the proposed PGIs are fundamentally different from the classic GIs in terms of generation and application.

GIs are generated through mesh-based parameterization algorithms, which are usually formulated as either a non-linear optimization problem that minimizes area and/or angle distortions [2, 28, 44, 41] or a non-linear PDE that iteratively deforms the input 3D shape to a target shape with constant Gaussian curvature [60, 15]. GIs are typically judged by the overall angle and area distortion, and applied to GPU-accelerated rendering and texture mapping (*e.g.*, in movies and video games). The mesh-based algorithms are able to compute high-quality GIs for 3D models with simple geometry and topology. However, increasing the complexity of geometry/topology often poses significant challenges to these methods. Furthermore, they only work for the manifold meshes with a single component, whereas the non-manifold models with multiple connected components are common in real-world applications. Last but not least, extending the mesh-based parameterization algorithms to point clouds is non-trivial due to their high reliance on the connectivity information provided by meshes.

Our method is data-driven and can work for arbitrary manifold and non-manifold models with single or multiple components. Since ParaNet makes no use of connectivity, it is ideal for processing point clouds. As an end-to-end learning framework, it is trained in an unsupervised manner. Moreover, it can be combined and jointly optimized with downstream task networks. Since PGIs can be seamlessly coupled with conventional 2D CNN architectures, they are particularly useful for visual analysis tasks, such as classification, segmentation, super-resolution and recognition, in which 2D CNNs have already demonstrated great potentials.

Due to these fundamental differences, we do not naïvely follow conventional GI metrics to measure PGIs. In our paper, we evaluate PGIs in terms of: 1) the information loss between the input point cloud and the PGI-induced point cloud; and 2) the performance of specific downstream applications when applying 2D CNNs to the generated PGIs.

In Figure 11, we provide more examples of the 2D embeddings and PGIs. The displayed models belong to the ModelNet40 [55] repository. We observe that ParaNet works well for diverse object categories.
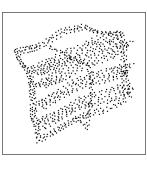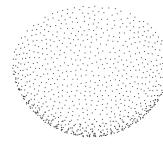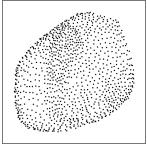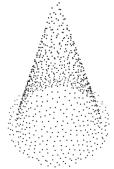
2. Details of Network Architectures
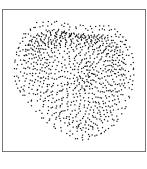
2.1 ParaNet
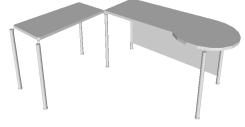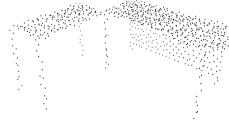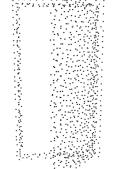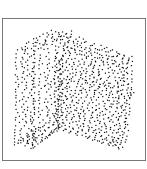
In our implementation, we employed the popular DGCNN [52] architecture for feature extraction of input point clouds. The extracted global feature for an input point cloud is a 512-dimensional feature vector, *i.e.*, $\mathbf{c} \in \mathbb{R}^{512}$. In the surface embedding module, each unfolding operator was implemented as a shared four-layer perceptron. The dimensions of the first and the second unfolding operator are $\{512 + 3, 256, 128, 64, 2\}$ and $\{512 + 2, 256, 128, 64, 2\}$, respectively. For the annealing regularization term in soft grid resampling, we initiated the learnable temperature coefficient as $\tau = 10^{-5}$. Besides, the number of nearest neighbors selected for each grid point was set as $K = 5$. In practice, we discover that the soft grid resampling module is not sensitive to the value of K due to the effective annealing process.

2.2 ParaNet-SC: Downstream Task Network for 3D Shape Classification

The ParaNet-SC framework tailored for 3D shape classification adopted the ResNet18 [12] architecture, which has been widely applied to a variety of image domain visual applications, as the backbone feature extractor. Following common notations, the standard ResNet18 feature encoder can be partitioned and packed into five sequential convolution stages, denoted as: {Conv-1, Conv-2, Conv-3, Conv-4, Conv-5}. Note that we dropped the max-pooling layer in the Conv-1 stage to enlarge the feature resolution.

Considering that the generated PGIs usually represent the original point clouds in a highly-redundant manner, it is necessary to deal with the information redundancy issue. Thus, we introduced the popular attention mechanism, as proposed in [53], which has already gained remarkable success in numerous image/video processing tasks. In [53], a spatial attention module (SAM) is applied to aggregate inter-spatial feature dependency and suppress the less informative image parts, and a channel attention module (CAM) is applied to exploit inter-channel relationships and emphasize the most discriminative feature subspace. Intuitively, the combination of SAM and CAM enables the network to learn *where* and *what* to emphasize or suppress, effectively enhancing the representation capability of the learned convolutional feature maps. Please refer to the

Category	3D Meshes	Point Clouds	2D Embeddings	PGIs
bookshelf				
bowl				
chair				
cone				
desk				
door				
guitar				

original paper [53] for complete and detailed descriptions of SAM and CAM. To further clarify the structure composition of

Category	3D Meshes	Point Clouds	2D Embeddings	PGIs
person				
plant				
sink				
stairs				
stool				

Figure 11. More results of the 2D embeddings and PGIs produced by ParaNet.

ParaNet-SC, we list all the included major components as well as the corresponding output dimensions in Table 5.

2.3 ParaNet-PU: Downstream Task Network for Point Cloud Upsampling

The ParaNet-PU framework is designed to achieve $4\times$ point cloud upsampling following a patch-based processing pipeline. Specifically, we tend to upsample a 256-point sparse patch to a 1024-point dense patch through ParaNet-PU. As described in the paper, we explored three different types of training strategies (*i.e.*, JO, Off-IO, and On-IO) for connecting ParaNet with a specific downstream task network. For the shape classification task, we can observe that the JO scheme outperforms the other two choices. Although joint optimization always results in higher information loss, *i.e.*, more points may be lost in the generated PGI, it benefits from end-to-end training in which the PGI representation can be adaptively adjusted to some extent, boosting the overall classification performance. Different from shape classification that is relatively less sensitive to information loss, point cloud upsampling highly relies on the original geometry and topology information provided by the input sparse point set. Even if only a few critical points are missing, it would be rather difficult to accurately infer the underlying surface. Thus, we adopted the On-IO scheme for training our ParaNet-PU framework, generating PGIs

Table 5. Components and outputs of ParaNet-SC.

Components	Outputs ([Channels, Height, Width])
PGI	[3, 128, 128]
Conv-1	[64, 64, 64]
SAM-1	[64, 64, 64]
Conv-2	[64, 64, 64]
SAM-2	[64, 64, 64]
Conv-3	[128, 32, 32]
SAM-3	[128, 32, 32]
Conv-4	[256, 16, 16]
CAM-4	[256, 16, 16]
Conv-5	[512, 8, 8]
CAM-5	[512, 8, 8]
Global Average Pooling	[512, 1, 1]
Fully Connected Layer	[40]

with the resolution of 128×128 for all training and testing patches with 256 points.

Technically, we started by feeding the input PGI into a series of convolutional layers with large sized filters followed by max-pooling operations to reduce feature resolution. We introduced self-attention, as proposed in [51], to build long-range point dependency and encode the global shape prior of the input patch. After that, we employed the back projection mechanism [11] to fully exploit the mutual relationships of low- and high-resolution feature maps. As investigated in [11], the back projection workflow involves the up-projection units (UPU) and the down-projection units (DPU). Following the original design, we sequentially organized the two types of projection units, alternating between the UPU and the DPU, which can be considered as a self-correcting learning procedure providing a beneficial error feedback mechanism. In Table 6, we summarize the major components and the corresponding output dimensions. As suggested, we concatenated the up-sampled feature maps produced by the three UPUs and then applied 1×1 convolutions to generate 3D Cartesian coordinates. In the end, we could easily reshape the predictions into a 2D array, representing the upsampled point cloud patch.

During training, we employed the Earth Mover's Distance (EMD) to measure the difference between upsampling results and ground truths. To promote the uniformity of the generated patches, we additionally imposed a point distribution constraint, expecting that the nearest neighbors are neither too close nor too far from each other. To achieve this, we adopted a modified *repulsion loss*, which was originally proposed in PU-Net [59]. Given an upsampled patch $\mathbf{X} = \{x_i\}_{i=1}^{U}$ and the corresponding ground truth patch $\mathbf{Y} = \{y_i\}_{i=1}^{U}$, we formulated the uniformity constraint in a fast-decaying manner as follows

$$\mathcal{L}_{uni} = \gamma \cdot \frac{1}{U} \sum_{i=1}^{U} -r(x_i) \cdot \exp(-\frac{r(x_i)^2}{2h^2}), \tag{9}$$

where $r(x_i)$ represents the Euclidean distance between x_i and its nearest neighbor, and γ controls the contribution of $\mathcal{L}_{uni}$ when combined with the EMD loss function for point generation supervision. Empirically, we set the parameter γ to be 0.01. Actually, the above constraint tends to push the nearest neighbor distance $r(x_i)$ to a fixed value of h, which is chosen as the average nearest neighbor distance in patch $\mathbf{Y}$ as follows

$$h = \frac{1}{U} \sum_{i=1}^{U} r(y_i). \tag{10}$$

To further boost the generation of uniformly distributed point clouds, we introduced side supervisions to enhance the learned intermediate feature representations. In our implementation, we applied additional 1×1 convolutions to the outputs of DPU-1 and DPU-2, predicting sparse patches with 256 points. Then we used farthest point sampling to downsample the corresponding ground truth patch with 1024 points into a uniform 256-point patch, which serves as the intermediate supervision information to guide the predicted side outputs using the weighted combination of EMD and uniformity constraint.

15

Table 6. Components and outputs of ParaNet-PU.

Components	Outputs ([Channels, Height, Width])
PGI	[3, 128, 128]
Conv (12×12)	[64, 64, 64]
Conv (8×8)	[128, 32, 32]
Self-Att	[128, 32, 32]
Conv (6×6)	[256, 16, 16]
Self-Att	[256, 16, 16]
UPU-1	[256, 32, 32]
DPU-1	[256, 16, 16]
UPU-2	[256, 32, 32]
DPU-2	[256, 16, 16]
UPU-3	[256, 32, 32]
Up-Concat	[768, 32, 32]
Conv (1×1)	[3, 32, 32]
Reshape	[3, 1024]

Table 7. Comparison of Different Point Feature Extractors for 3D Shape Classification.

Method	Rep Acc (CD)	Cls Acc (%)
ParaNet-SC-DGCNN (JO)	2.32×10^{-6}	93.1
ParaNet-SC-PointNet (JO)	9.61×10^{-6}	93.1

Table 8. Comparison of Different Point Feature Extractors for Point Cloud Upsampling.

Method	Rep Acc (CD) (10^{-8})	P2F (10^{-3})	CD (10^{-3})	HD (10^{-3})
ParaNet-PU-DGCNN (On-IO)	2.09	2.26	0.28	4.44
ParaNet-PU-PointNet (On-IO)	7.15	2.27	0.28	4.49

3. Backbone Point Feature Extractor

In our paper, we employed DGCNN [52] as the backbone point feature extractor of ParaNet. Actually, we argue that DGCNN can be seamlessly replaced by any other kind of deep set architecture, and the overall performance over a specific downstream application is dominated by the task network and less sensitive to the point feature extractor. To empirically demonstrate this point, we replaced DGCNN [52] with PointNet [35] in the ParaNet for generating PGIs while maintaining the subsequent components. In Tables 7 and 8, we compared the data representation accuracy (Rep Acc) under the Chamfer distance (CD) metric and the overall task performance of DGCNN-driven (*i.e.*, ParaNet-SC/PU-DGCNN) and PointNet-driven (*i.e.*, ParaNet-SC/PU-PointNet) processing pipelines. We can observe that although PointNet, a backbone point encoder which is not as powerful as DGCNN, results in some decrease in the data representation accuracy, the overall performances of the downstream tasks are basically not affected, which implies that the proposed PGI-driven point cloud processing framework is not limited by a specific type of point feature extractor. In practice, we can expect to focus on exploiting and designing generic CNN architectures to promote various point cloud applications.